Science Advances
AAAS

advances.sciencemag.org/cgi/content/full/7/1/eabe4310/DC1

Supplementary Materials for

Nanoscale chromatin imaging and analysis platform bridges 4D chromatin organization with molecular function

Yue Li, Adam Eshein, Ranya K.A. Virk, Aya Eid, Wenli Wu, Jane Frederick, David VanDerway, Scott Gladstein, Kai Huang, Anne R. Shim, Nicholas M. Anthony, Greta M. Bauer, Xiang Zhou, Vasundhara Agrawal, Emily M. Pujadas, Surbhi Jain, George Esteve, John E. Chandler, The-Quyen Nguyen, Reiner Bleher, Juan J. de Pablo, Igal Szleifer, Vinayak P. Dravid, Luay M. Almassalha, Vadim Backman*

*Corresponding author. Email: v-backman@northwestern.edu

Published 1 January 2021, *Sci. Adv.* **7**, eabe4310 (2021)
DOI: 10.1126/sciadv.abe4310

The PDF file includes:

Figs. S1 to S9
Table S1
Sections S1 to S3
Legends for movies S1 to S5
References

Other Supplementary Material for this manuscript includes the following:

(available at advances.sciencemag.org/cgi/content/full/7/1/eabe4310/DC1)

Movies S1 to S5

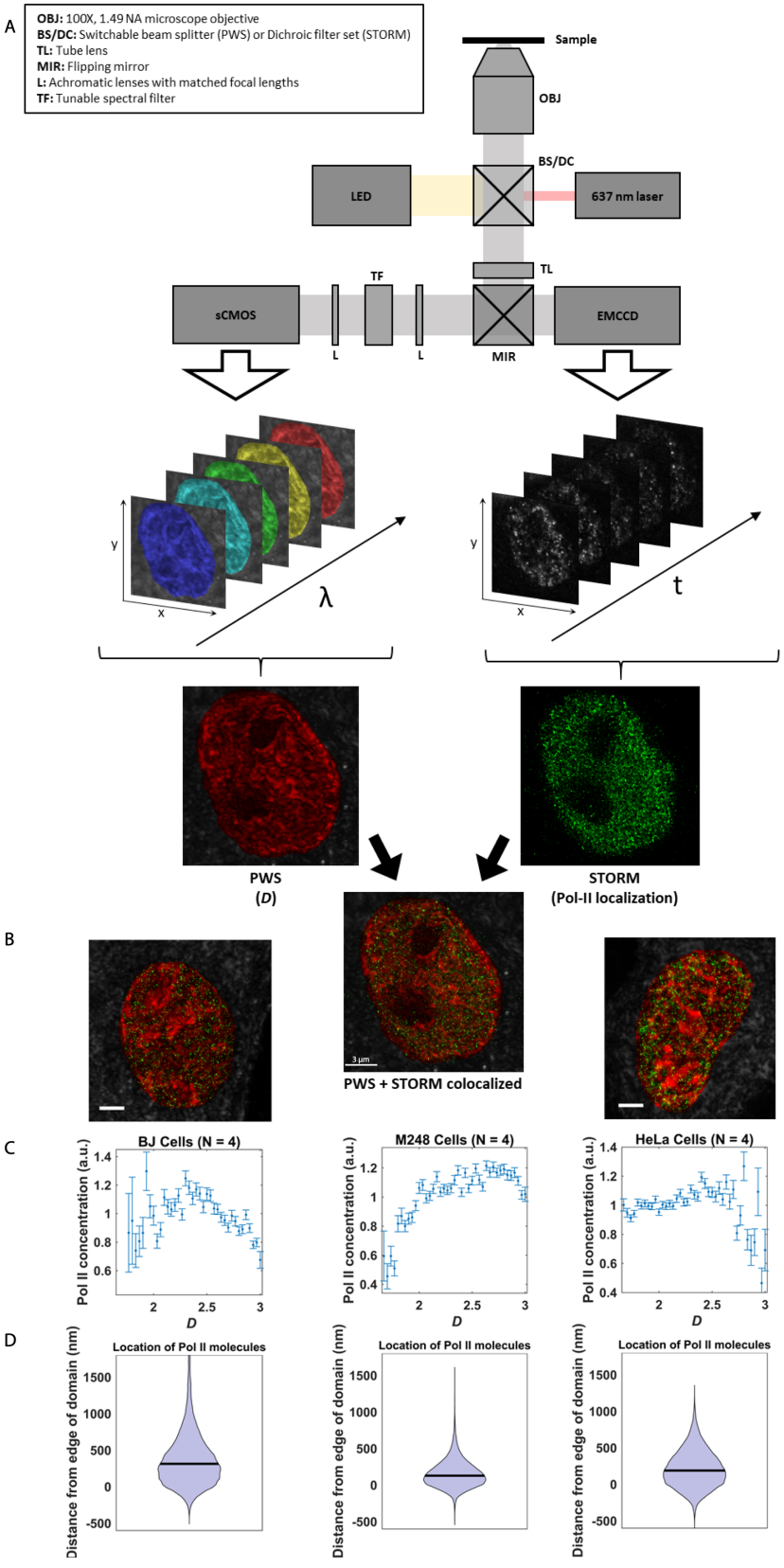
A
OBJ: 100X, 1.49 NA microscope objective
BS/DC: Switchable beam splitter (PWS) or Dichroic filter set (STORM)
TL: Tube lens
MIR: Flipping mirror
L: Achromatic lenses with matched focal lengths
TF: Tunable spectral filter
Sample
OBJ
BS/DC
LED
637 nm laser
TL
TF
sCMOS
EMCCD
L
L
MIR
y
x
λ
y
x
t
PWS
(D)
STORM
(Pol-II localization)
B
3 μm
PWS + STORM colocalized
C
BJ Cells (N = 4)
M248 Cells (N = 4)
HeLa Cells (N = 4)
Pol II concentration (a.u.)
D
D
Location of Pol II molecules
Distance from edge of domain (nm)

Fig. S1. Multi-modal STORM-PWS optical microscopy schematic. (**A**) The optical schematic of the combined STORM and PWS microscopy instrument. During PWS acquisition, broadband light from an LED is introduced onto the sample via a 50/50 beam splitter. The light is collected and sent to an EMCCD or sCMOS camera though a tunable spectral filter. During STORM acquisition, 637 nm monochromatic red laser light is introduced onto the sample via a dichroic filter set. Fluorescence light is collected and sent to an EMCCD camera. For PWS, multiple spectrally resolved images are acquired and analyzed to create a map of *D*. For STORM, multiple frames of fluorescence emission events are acquired and analyzed to reconstruct a super-resolution fluorescence image of labeled Pol-II. The reconstructed STORM image and calculated *D* map are finally combined into a single image. (**B**) Representative STORM-PWS images from differentiated BJ fibroblast cells, A2780.M248 (M248) ovarian cancer cells and HeLa cells. The intensity of red represents chromatin packing scaling measured by PWS, and green shows the locations of Pol-II molecules visualized by STORM. Scale bar: 3 μm. (**C**) While there is considerable variation between cell types, the nonmonotonic relationship between Pol-II density and local *D* is the same for all cell lines studied. (**D**) Distribution of distances between highly enriched Pol-II regions and PD boundaries. In all three cell lines, Pol-II tends to group near the edges of PDs.

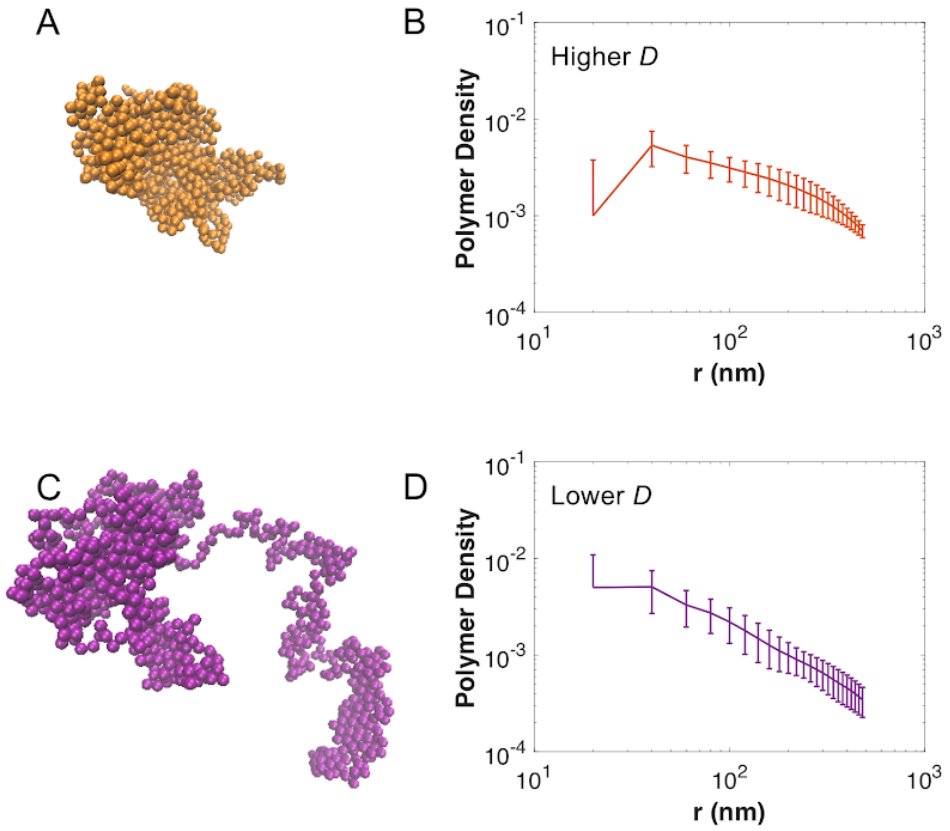

Fig. S2. Polymer density decays slower with radial distance for higher *D* polymers. Renderings of self-attracting homopolymers with (**A**) higher ($D = 2.41$) and (**C**) lower ($D = 1.95$) packing scaling. Analysis of average radial polymer density (i.e. mass contained in a sphere with increasing radius r) for the higher *D* polymer (**B**) exhibits a slower decay than for the lower *D* polymer (**D**). Polymer density was averaged from density scaling behavior surrounding 25 randomly selected monomers.

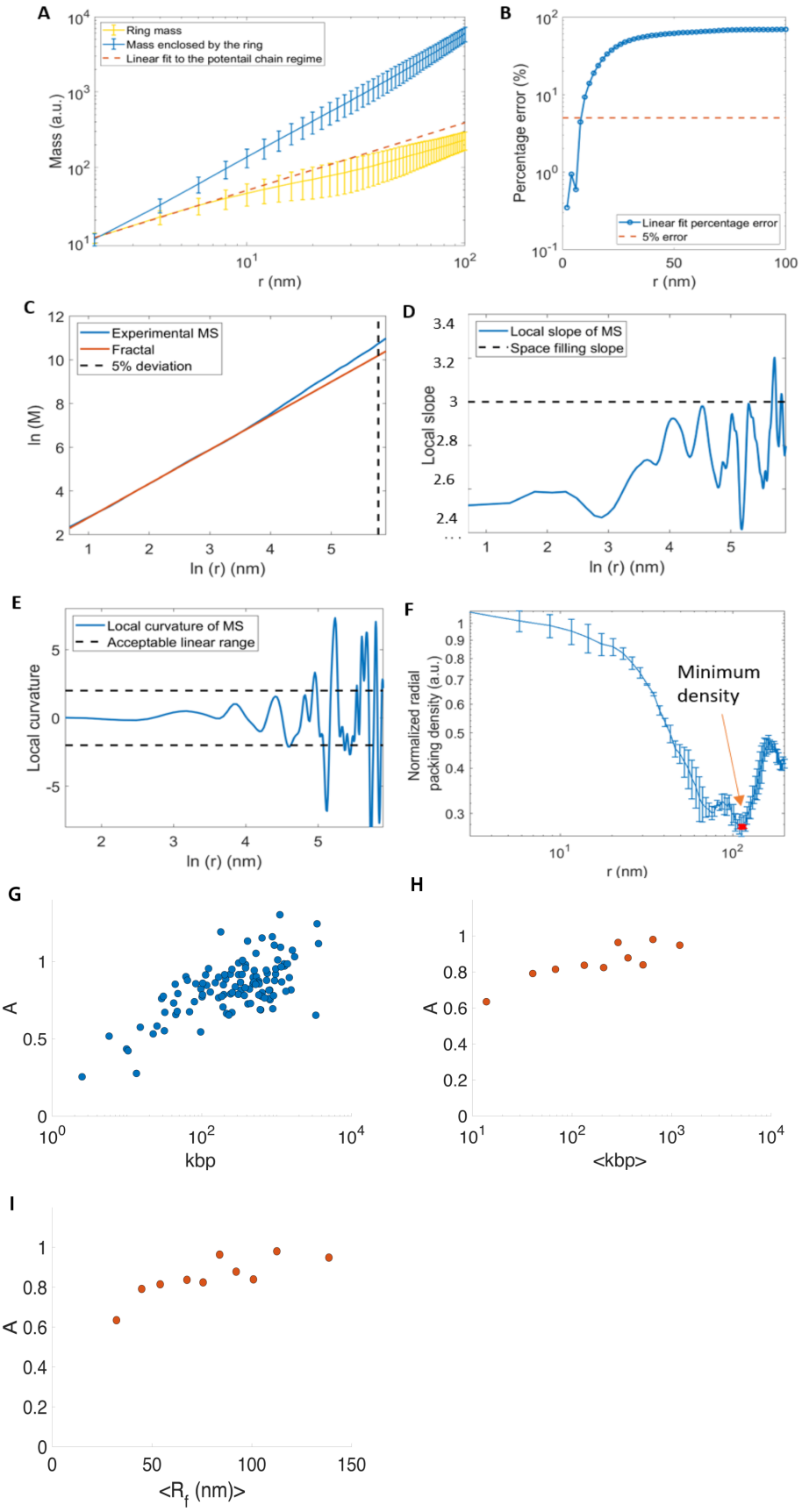
A
Ring mass
Mass enclosed by the ring
Linear fit to the potentail chain regime
Mass (a.u.)
r (nm)
B
Percentage error (%)
Linear fit percentage error
5% error
r (nm)
C
Experimental MS
Fractal
5% deviation
ln (M)
ln (r) (nm)
D
Local slope of MS
Space filling slope
Local slope
ln (r) (nm)
E
Local curvature of MS
Acceptable linear range
Local curvature
ln (r) (nm)
F
Minimum density
Normalized radial packing density (a.u.)
r (nm)
G
A
kbp
H
A
<kbp>
I
A
<R_f (nm)>

Fig. S3. Description of ChromSTEM PD analysis. Chromatin chain regime on the ring mass scaling curve and determining the packing domain radius (R_f) and D from ACF. The mass in the mass scaling curve, as shown in Fig. 2D is defined as the mass enclosed by a ring with radius r, also shown here in the blue line in (**A**)**.** Alternatively, for the 1D case, the mass is the mass located on the ring with radius r, shown as the red line in (**A**). The ring mass scaling curve is indicative of a third regime besides fractal regime and uncorrelated supra-domain region. We performed a linear regression on the ring mass scaling curve to the first 6 nm range and defined the upper limit of this range to be the length scale where the ring mass scaling first exceeds 5% deviation from the linear regression, as shown in (**B**). The upper bound for the region is calculated to be 8.24 nm, consistent with the radius of the chromatin chain reported in the earlier ChromEMT work (*8*). However, as the nominal resolution is 2 nm, the chromatin chain region consists of only four data points on the ring mass scaling curve (three data points on log-log scale, as the first point r= 0 is not defined), and only three data points on the mass scaling curve (two data points on log-log scale, the first point r = 0 is not defined), and thus insufficient to unequivocally demonstrate different between chromatin packing of the chromatin chain and the fractal domain. Three criteria are considered to calculate R_f from the mass-scaling (MS) curve for individual domains. (**C**) Linear regression was conducted for the mass scaling curve between 2 nm to 32 nm. The spatial separation where the linear regression has a 5% deviation from the experimental MS curve (dashed line) is defined as R_{fit}. (**D**) The local slope of the experimental MS curve was estimated by moving window linear regression (5 pixels per window). The spatial separation where the local slope reaches 2 (dashed line) is defined as $R_{space\_filling}$. (**E)** The local curvature of the experimental MS curve was again calculated by moving window linear regression on the local slope curve (5 pixels per window). The spatial separation where the absolute value of the local curvature exceeds 2 (dashed line) is defined as R_{non_linear} . (**F**) Chromatin packing density radial profile. From the center to the domain boundary, the packing density of chromatin fibers decreases gradually. We define the spatial separation where the packing density reaches its minimum as $R_{min\_density}$. Furthermore**,** R_f is defined as the smallest value among R_{fit}, $R_{space\_filling}$, R_{non_linear}, and $R_{min\_density.}$ For cases where either R_{fit}, $R_{space\_filling}$, or R_{non_linear} do not exist, we use infinity for that parameter. (**G**) Dependence of packing efficiency factor A describing the relationship between CVC and D on genomic size of PDs in kbp plotted on a semi-log scale. Genomic size in kbp was estimated by first determining N_f, the number of elementary units of size R_{min} = 10nm in a given PD using the equation $N_f = CVC * \left(\frac{R_f}{R_{min}}\right)^3$. The number of base pairs within each elementary unit was then estimated to be 1.9 kbp calculated by dividing the estimated median genomic size of a PD (352.6 kbp) by the calculated median N_f (187). There is a positive correlation between genomic size of each domain and packing efficiency factor. (**H-I**) Analysis of A for PDs binned into 10 equal quantiles based on R_f. (**H**) Dependence of A on average genomic size of binned PDs shows a positive correlation between average genomic size of binned domains and A. (**I**) Relationship between average binned R_f (in nm) and A.

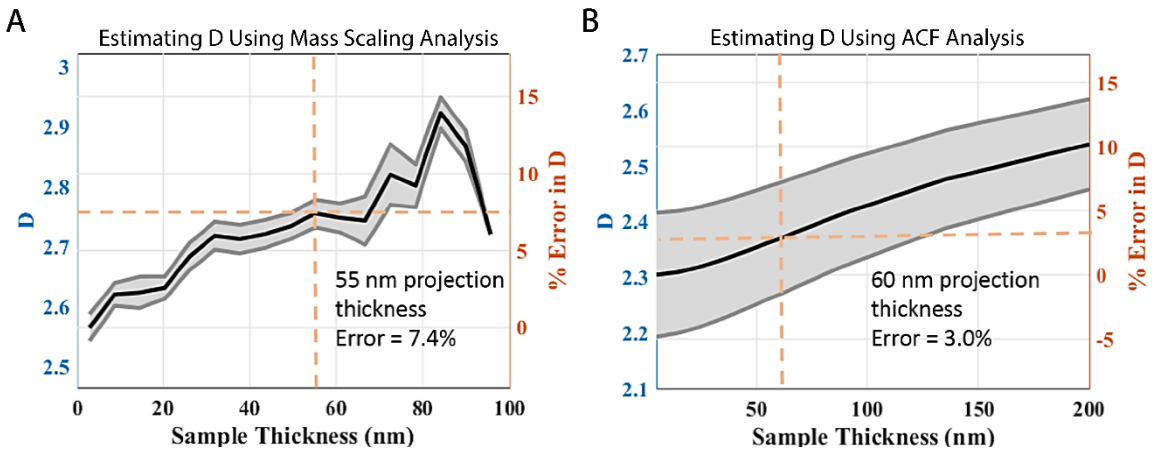

Fig. S4. Estimating *D* from the projection of chromatin at varying thicknesses using mass scaling versus ACF analysis. For the mass scaling analysis, we created a series of projection images with incremental thickness by projecting the virtual 2D slices of the 3D tomograms of A549 chromatin masks, respectively. Mass scaling curves were calculated first. Then linear regression was performed within 11.6 nm to 50 nm. For the ACF analysis, a random media was generated with 600^3 voxels, 5nm pixel size along each dimension and had a true fractal dimension of 2.3. The generated medium was 4 μm in each dimension to ensure the fractal range could be fit given the numerical limitations. Next, 2D projections of the 3D volume were averaged, and the slope of their ACF was fit to a power law. All fits were performed within the same range from 50 to 100nm. For both analyses, the average *D* for each projection of varying sample thickness is plotted. For mass scaling analysis (left), the estimated *D* is 7.4% larger than the ground truth for a 55 nm thick projection while the ACF analysis (right) gives only a 3% error in *D* for a comparable 60 nm thick projection image of chromatin.

BJ fibroblast cells

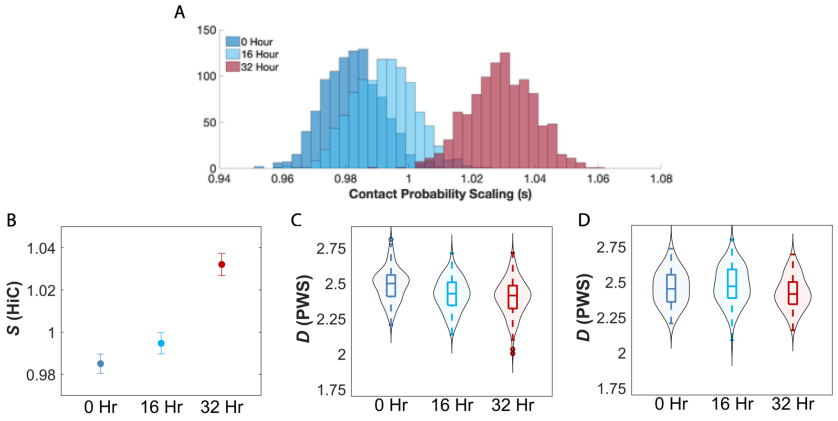

A549 cancer cells

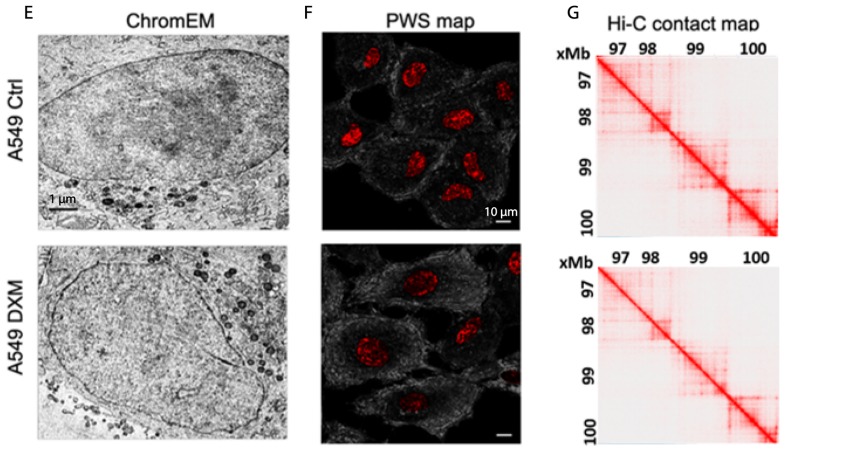

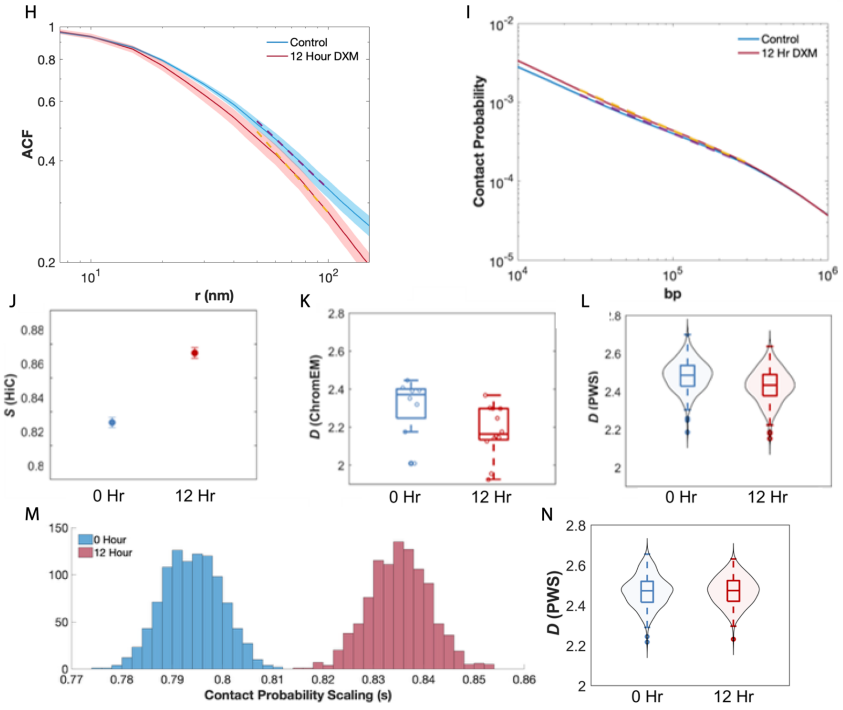

Fig. S5. Measuring chromatin packing scaling and contact probability scaling alterations induced by dexamethasone (DXM) treatment in BJ differentiated fibroblast and A549 cancer cells. (**A-B**) Contact probability scaling analysis as analyzed by moving-window linear regression (**A**) and classical linear regression (**B**) analyses for BJ cells treated with DXM for 0, 16, and 32 hours. For (**A**), we assume the linear regression fit used to calculate contact probability scaling follows a normal distribution $\mathcal{N}(\mu_s, \sigma_s)$ where mean contact probability scaling, μ_s, is the slope of the regression and standard deviation, $\sigma_s$is the root-mean-square error (RMSE) of the residuals. Contact probability scaling is significantly different between control, and 16-hour and 32-hour DXM treated BJ cells ($P < 0.001$). (**C-D**) PWS analysis of BJ cells at 0, 16, and 32 hour time points for untreated cells (**C**) and DXM treated cells (**D**). (**C**) Chromatin packing scaling D measured in untreated live BJ cells shows no observable change in D over a 16-hour period and only a small decrease in D over a 32-hour period that is not statistically significant ($P > 0.05$). (**D**) Using double-sided student-t-test, $P < 0.005$ for DXM treated cells at 16 and 32 hour time points. (**E-F**) nano-ChIA platform characterization of A549 chromatin structure with and without DXM treatment. From left to right: TEM images of chromatin structure with ChromEM staining, scale bar: 1μm. PWS map of chromatin packing scaling, scale bar: 10 μm. Qualitatively, both ChromTEM and PWS images show that DXM treatment homogenizes chromatin packing. (**G**) Hi-C contact map of human chromosome 1 rendered with 5kb resolution for the control and DXM treated A549 cells. (**H**) ACF analysis of ChromTEM images of A549 cells. The average ACF of the control group (blue) is significantly different from the average ACF of the treated group (red). The shaded regions represent standard errors. D was calculated inside the first fractal domain (50 nm to 100nm) by performing a linear regression fit to the ACF in the log-log scale. (**I**) Contact probability analysis performed on whole-genome intrachromosomal Hi-C contact data. Contact probability scaling (s) was calculated from a linear regression fit (dotted line) of the contact probability curve in the log-log scale between genomic distance $10^{4.4}$ and $10^{5.5}$ bp. (**J-L**) Chromatin packing scaling alterations induced by DXM treatment measured using ACF analysis of TEM images and PWS and changes in contact probability scaling of Hi-C contact data. Across the platform, consistent changes were observed in chromatin packing scaling upon treatment. Using double-sided student-t-test, $P = 0.051$ for ChromTEM, $P < 0.005$ for PWS. (**M**) Comparing distributions of contact probability scaling for A549 cells calculated from analysis of Hi-C contact matrices. We assume the linear regression fit used to calculate contact probability scaling follows a normal distribution $\mathcal{N}(\mu_s, \sigma_s)$ where mean contact probability scaling, μ_s, is the slope of the regression and standard deviation, $\sigma_s$is the root-mean-square error (RMSE) of the residuals. Contact probability scaling is significantly different between control, and 12-hour DXM treated A549 cells ($P < 0.001$). (**N**) Chromatin packing scaling D measured in untreated live A549 cells at 0 and 12 hours shows no observable change in D at time points comparable to DXM treatment, which showed a statistically significant decrease in D after 12 hours of treatment (Fig. S5L).

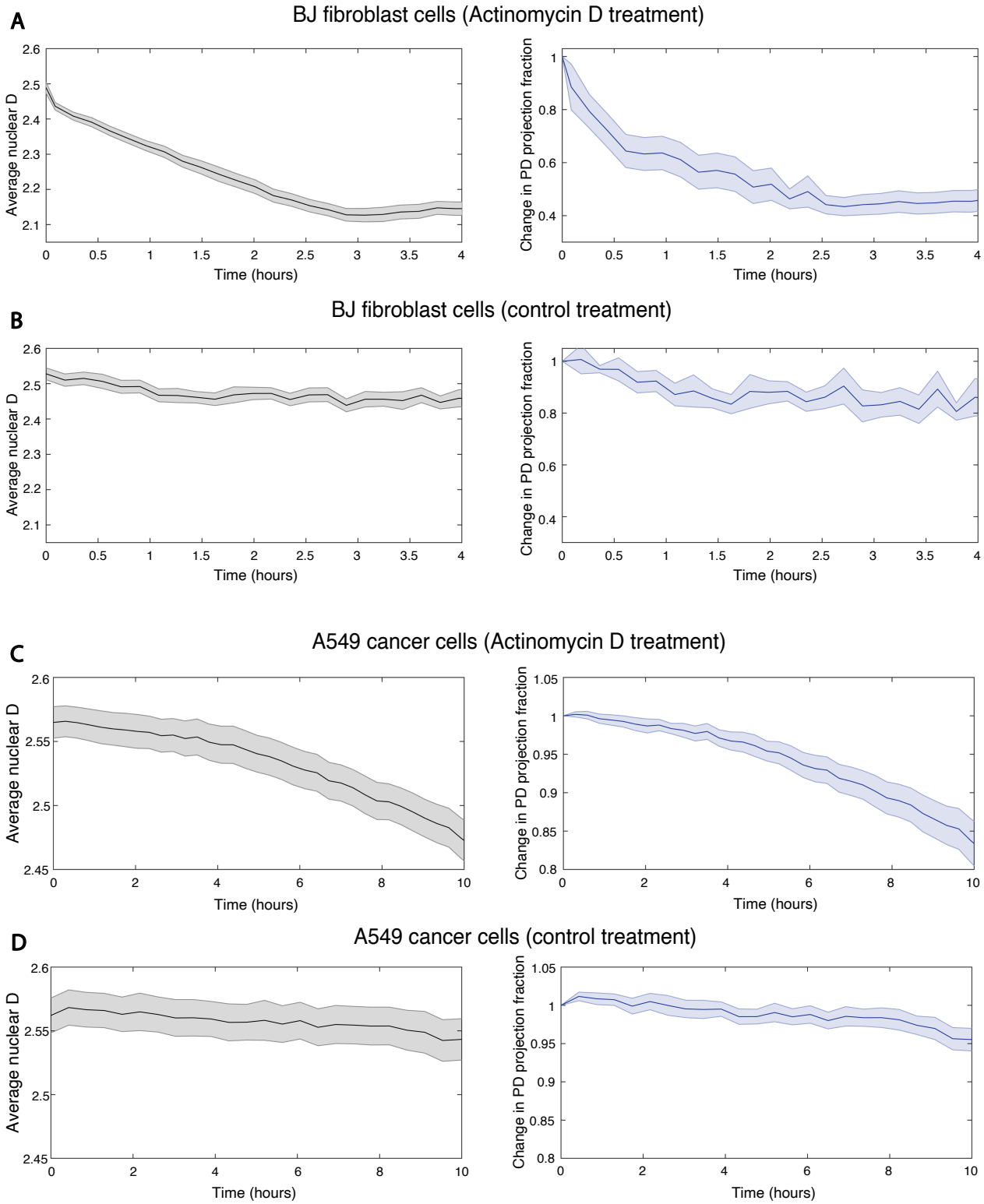

Fig. S6. Quantifying changes in chromatin structure upon treatment of cells with Actinomycin D. (**A**) BJ cells were continuously monitored with PWS for four hours after treatment with Act-D. (Left) Average nuclear *D* drops significantly over the first three hours and then appears to plateau. (Right) There is a significant initial drop in the projection of the PD

projection fraction. Notably, the PD projection fraction never drops below ~40% of its initial value. It also should be noted that, as Act-D inhibits all transcription processes, the treated cells eventually undergo apoptosis. (**B**) Vehicle control-treated BJ cells were monitored continuously with PWS over four hours (Left). Average nuclear *D* and (Right) projection of PD projection fraction do not change significantly (~3% for *D* and ~14% for PD projection fraction) over four hours compared to Act-D treated cells (Fig. 4G-4H and S6A). (**C**) A549 cells were continuously monitored with PWS over a ten-minute period after treatment with Act-D. (Left) Average nuclear *D* and (Right) PD volume fraction both decrease significantly over this time period. (**D**) Vehicle control-treated A549 cells were monitored continuously with PWS over ten minutes (Left) Average nuclear *D* and (Right) projection of PD projection fraction do not change significantly (< 1% for *D* and ~4% for PD projection fraction) over ten minutes compared to Act-D treated cells (Fig. S6C).

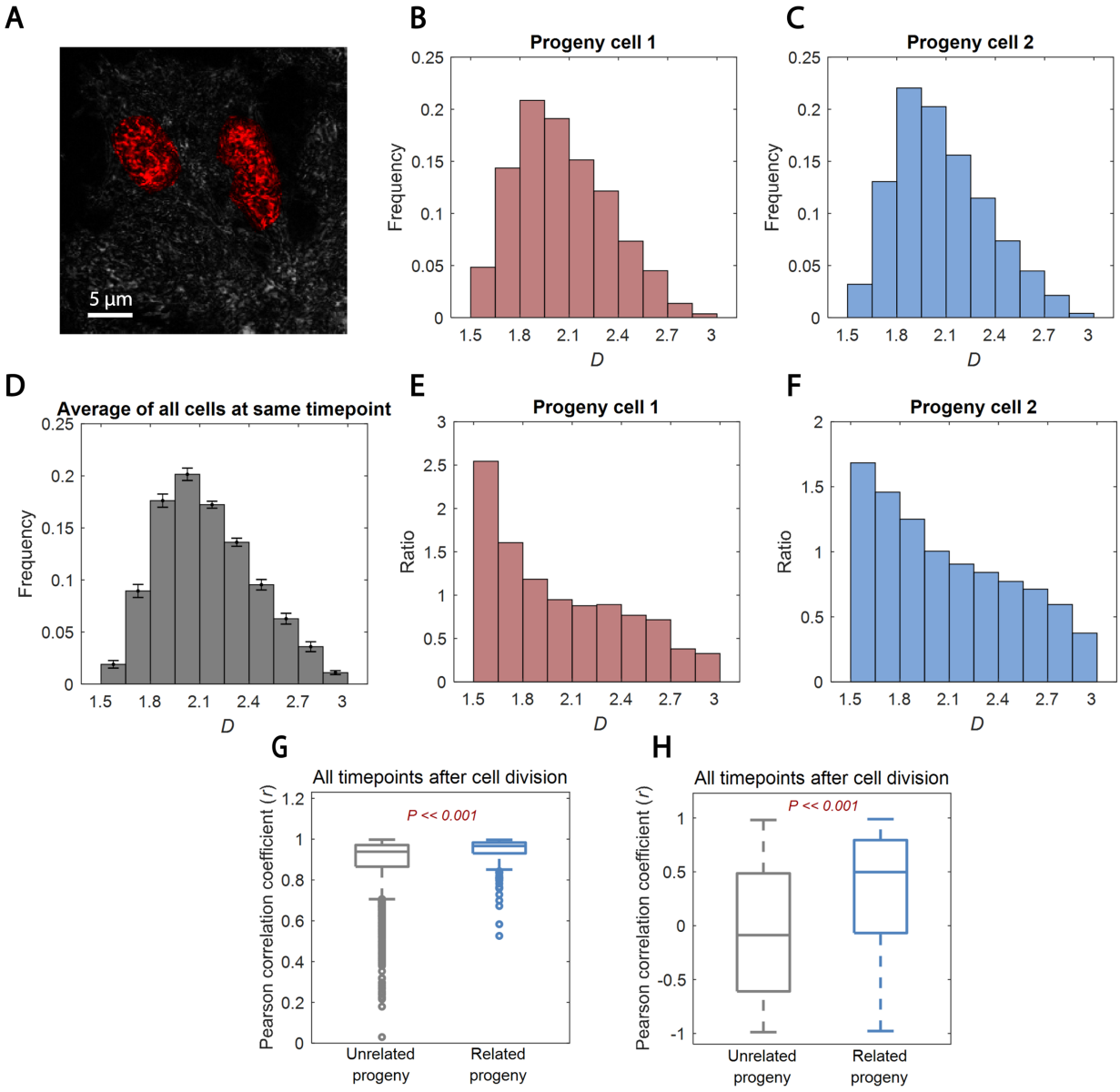

Fig. S7. Histogram calculations of *D* distribution for heritability analysis. (**A**) PWS *D* map of two HCT116 cells originating from the same progenitor cell imaged 5 hours after completion of cell division. (**B&C**) Histogram of *D* values derived from the two HCT116 cells shown in (a). (**D**) The average histogram representing the average *D* distribution of all cells imaged 5 hours after cell division. (**E&F**) Resulting histogram ratio after the histograms shown in (b) and (c), representing the *D* distributions of individual progeny cells, are divided by the average histogram of all cells at that time point distribution as shown in (**D**). This ratio of histograms represents the deviation of each cell's *D* distribution from the population mean. (**G**) Distribution of Pearson correlation coefficients comparing the unnormalized histograms of related and unrelated progeny at all time points after cell division. Although unrelated cells have a relatively high correlation coefficient ($r > 0.5$), the *D* distribution of cells originating from the same progenitor is significantly more correlated. (**H**) Distribution of Pearson correlation coefficients calculated from the normalized ratio-histograms of related and unrelated progeny at all time points after cell division.

As each cell's histogram is normalized by the mean *D* distribution at that time point, unrelated cells are less correlated, while related progeny cells are significantly more correlated.

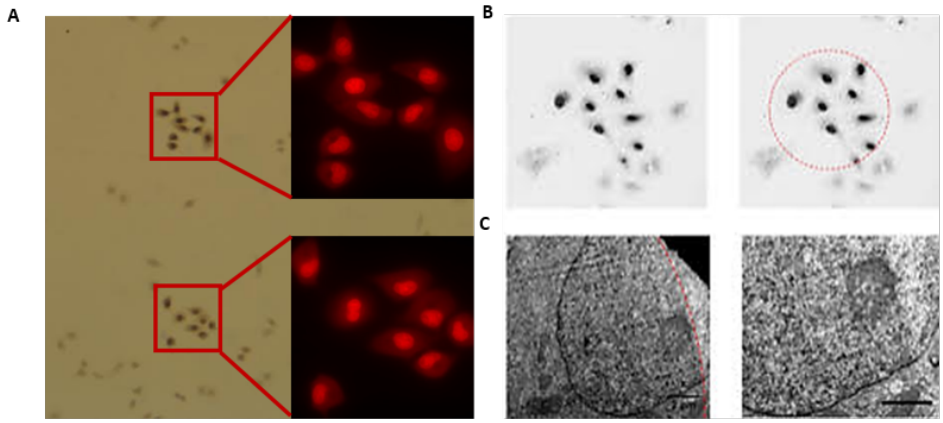

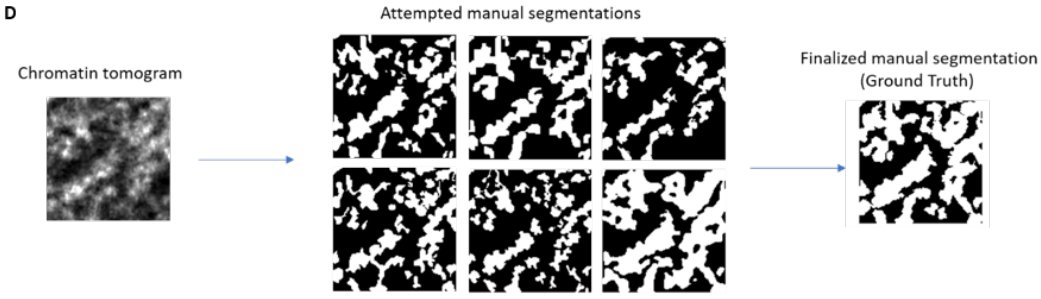

	1	2	3	4	5	6	7	8	9	10	11	12
Contrast mode	BF	BF	BF	BF	BF	BF	DF	DF	DF	DF	DF	DF
CLAHE block size	100	120	75	100	120	75	100	120	75	100	120	75
Thresholding algorithm	Li	Li	Li	Otsu	Otsu	Otsu	Li	Li	Li	Otsu	Otsu	Otsu
F1 score	**0.8709**	**0.8607**	**0.8705**	**0.8826**	**0.8733**	**0.8826**	**0.8773**	**0.8811**	**0.8801**	**0.8809**	**0.8837**	**0.8822**

Fig. S8. ChromEM staining and segmentation analysis reveals DNA distribution inside A549 cell nuclei. Draq5^{TM} was used to label the double-strand DNA inside the nucleus. Upon excitation, the Draq5 molecule will release single oxygen, which reacts with the diaminobenzidine-tetrahydrochloride (DAB) solutes to form electron-dense precipitates. The DAB precipitates are further enhanced by reduced osmium to create contrast for EM imaging. As shown in the fluorescent images of A549 labeled by Draq5 (**A**) and bright-field optical images of the resin-embedded cells, only cells with photo-oxidation show darker contrast (**B**). (**C**) The staining area has high precision, as indicated by a partially photo-oxidized cell. Within the nucleus, the boundary of the stained area follows the shape of the light spot. (**D**) In the automatic chromatin mask segmentation algorithm, three parameters, contrast mode, CLAHE block size, and thresholding algorithm, need to be optimized for best segmentation accuracy quantified by F1 score. In six independent analysis, we manually segmented the chromatin mask from the same tomogram. We averaged all the masks, and pixels with values greater than 0.2 were considered chromatin, while pixels with values smaller than 0.2 were considered not chromatin. The finalized manual segmentation was used as the ground truth. Either bright field (BF) or dark field (DF) can be used in contrast mode to initiate segmentation. We chose three block size (in pixels), 75, 100, and 120,

for local contrast enhancement (CLAHE), and employed either Li's or Otsu's thresholding algorithm in FIJI. In combination, we experimented with 12 different sets of parameters. We calculated the F1 score for each set of parameters and determined the optimized parameters are DF as contrast mode, 120 pixels for CLAHE, and Otsu's algorithm.

Table S1. Descriptions and values of CPMC model parameters.

FIXED PARAMETERS	DESCRIPTION	VALUE ($\phi = 0$)
k_t^{ns}	Association rate constant for nonspecific TF-DNA binding	4.9×10^4 $mM^{-1}s^{-1}$
k_f^{ns}	Association rate constant for nonspecific Pol-II-DNA binding	3.6×10^4 $mM^{-1}s^{-1}$
$K_{D,TF}^{ns}$	Dissociation constant for nonspecific TF-DNA binding	1 mM
$K_{D,RNAp}^{ns}$	Dissociation constant for nonspecific Pol-II-DNA binding	1 mM
k_t	Association rate constant for TF-promoter binding	0.05×10^6 $mM^{-1}s^{-1}$
k_f	Association rate constant for Pol-II-Complex I binding	0.03×10^6 $mM^{-1}s^{-1}$
k_o	TF-promoter dissociation rate	1.0 s^{-1}
$K_{D,TF}$	Dissociation rate for TF-promoter binding	1 nM
$K_{D,RNAp}$	Dissociation rate for Pol-II-promoter binding	1 nM
k_m	Transcription rate of Pol-II	0.001 s^{-1}
γ	Nuclear export rate of mRNA	8×10^{-4} s^{-1}
ν	mRNA degradation rate	3×10^{-4} s^{-1}
r_{min}	Lower length scale of chromatin self-similarity	1 nm
σ^2	Variance of crowding density ϕ within a nucleus of average crowding density $\phi_{in,0}$	$\phi_{in,0}(1 - \phi_{in,0})$
L	Average number of base pairs in each gene	6 Kbp

UNFIXED PARAMETERS	DESCRIPTION	VALUE
r_{in}^{0}	Radius of interaction volume for single base pair	15 nm
N_f	Genomic size of upper length scale of chromatin self-similarity	10 Kbp
$\phi_{in,0}$	Average crowding density $\phi_{in,0} = \phi_0 + (1 - \phi_0)\phi_{MC}$	$\phi_0 = 32\%\ v/v$ (from ChromEM) $\phi_{MC} = 10\%\ v/v$ (mobile crowder estimate) $\phi_{in,0} = 38.8\%\ v/v$
$[C]_{tot}$	Total concentration of transcription complexes	[0.01nM, 0.1nM]

Section S1. Descriptions of SI videos

SI Video 1 – Single BJ cell treated with Dexamethasone measured with PWS for 32 hours. The average nuclear *D* of this cell is shown in Fig. S8.

SI video 2 – HCT 116 cancer cells measured by PWS every 15 minutes during mitosis. Data collected from this cell is shown in Fig. 5.

SI video 3 – HCT 116 cancer cells measured by PWS every 15 minutes during mitosis. Data collected from this cell is shown in Fig. 5.

SI video 4 – Tomography reconstruction of an interphasic A549 cancer cell.

SI video 5 – Volume rendering from tomography of the cell in SI video 4.

Section S2. ChromEM sample preparation, imaging, and tomography reconstruction

ChromEM sample preparation

For the EM experiments, all the cells were prepared by the ChromEM staining protocol (*8*). Hank's balanced salt solution without calcium and magnesium was used to remove the medium in the cell culture. Two-step fixation using EM grade 2.5% glutaraldehyde and 2% paraformaldehyde in 0.1M sodium cacodylate buffer (EMS) was performed: 1. Fixation at room temperature for 10 minutes. 2. Continuous fixation on ice for 1 hour with a fresh fixative. The cells were kept cold from this step either on ice or on a cold stage, and the solution was chilled before use. After

fixation, the cells were thoroughly rinsed by 0.1M sodium cacodylate buffer, blocked with potassium cyanide (Sigma Aldrich) blocking buffer for 15 minutes, and stained with DRAQ5™ (Thermo Fisher) with 0.1% saponin (Sigma Aldrich) for 10 minutes. The excessive dye was washed away using a blocking buffer. The cells were bathed in 3-3' diaminobenzidine tetrahydrochloride (DAB) solution (Sigma Aldrich) during photobleaching.

A Nikon inverted microscope (Eclipse Ti-U with the perfect-focus system, Nikon) with Cy5 filter sets were employed for photo-bleaching while the cells were kept cold on a custom-made wet chamber with humidity and temperature control. 15 W Xenon lamp and the red filter was used as the source of epi-illumination. With 100x objective, each spot was photo-bleached for 7 min, and fresh DAB was added to the dish for every 30 minutes. After photo-bleaching, the excessive DAB was washed away by 0.1 M sodium cacodylate buffer, and the cells were stained with reduced osmium (2% osmium tetroxide and 1.5% potassium ferrocyanide, EMS) for 30 minutes on ice to further enhance contrast. Following heavy metal staining, the cells were rinsed by DI, serial ethanol dehydrated, and brought back to room temperature in 100% ethanol. The standard procedure of infiltration and embedding using Durcupan™ resin (EMS) was performed. The flat embedded cells were cured at 60°C for 48 hours. The precision of the staining was tested for the entire photo-bleached cells and partially photo-bleached cells (Fig. S8A-S8C).

Two kinds of sections were made using an ultramicrotome (UC7, Leica). For the tomography, 100 nm thick resin sections were cut and deposited onto a copper slot grid with carbon/formvar film (EMS). For investigating the chromatin structure difference with and without dexamethasone treatment, 50 nm thick resin sections were made and deposited onto copper 200 mesh grid with carbon/formvar film (EMS). The grids were plasma-cleaned by a plasma cleaner (Easi-Glow, TED PELLA) prior to use. No post staining was performed, but 10 nm colloidal gold particles were added to the 100 nm thick samples on both sides as fiducial markers for the tomography.

Electron microscopy imaging and tomography reconstruction

A 200 kV STEM (HD2300, HITACHI) was employed for tomography data collection. High angle annular dark-field (HAADF) imaging contrast was used in the tilt series. In order to reduce the missing wedge, tilting series from – 60° to 60° on two perpendicular axes were recorded manually, with 2° step size. The pixel dwell time was kept small (~5 μs) to prevent severe beam damage during imaging. For the thin sections, a TEM (HT7700, HITACHI) was operated at 80 kV in the bright field to capture high contrast chromatin data.

For the STEM HAADF tilt series, the images were aligned using IMOD with fiducial markers (*50*). 40 iterations of a penalized maximum likelihood (PML) algorithm with non-negativity constraints in TomoPy (*51*) was employed for tomography reconstruction for each axis. The two reconstructed tomogram sets were re-combined in IMOD to further suppress the artifacts introduced by the missing cone. A nominal voxel size of 2.9 nm was used in the tomography to resolve individual nucleosomes. The 3D volume rendering was conducted using Volume Viewer in FIJI (*52*). The DNA density was used to generate color-coded nucleosome configurations, with green color dictates the lowest density, and red dictates the highest density. The chromatin binary

masks were employed to generate the surface of supranuclesomal structures. The videos of example tomography and volume rendering can be found in Movie S4, S5.

Section S3. Calculation of chromatin packing scaling (*D*) from spectral variance (Σ^2) measured by PWS

Mathematical description of chromatin within the fractal regime by the autocorrelation function

As suggested by the ChromSTEM experiment, chromatin is likely to form a fractal structure within packing domains (PDs). Within the fractal regime, the genomic size of the chromatin (N_f) scales up with its physical size R_f following a power-law relationship (*53*).

$$N_f = \left(\frac{R_f}{l_{min}}\right)^D \quad [1]$$

D is the chromatin packing density scaling (fractal dimension), l_{min} ~ 1 nm is the radius of the fundamental structural unit of chromatin, the nucleotide base pair, R_f is the upper bound of the power-law regime which represents the radius of the PD. Outside the upper bound, chromatin packs in an uncorrelated fashion and form supra-domains with a packing scaling of 3.

The autocorrelation function (ACF) representing chromatin mass density within the fractal regime adopts a power-law function, with the same power exponent *D*. However, a strict power-law function approaches infinity at the origin, a behavior that is not physical, as the smallest structural unit of chromatin are nucleotides which have a finite size. Additionally, the true ACF of a single PD gradually decays to zero. Thus, a modified power-law ACF (B_ρ) was used to include a lower and upper length limit to the power-law regime, and allow for both continuity and differentiability for all length scales (*54, 55*), as shown in equation [2]:

$$B_\rho(r, D_B, l_{min}, l_{max}) = \sigma_\rho^2 \frac{D_B - 3}{{l_{max}}^{D_B-3} - {l_{min}}^{D_B-3}} r^{D_B-3} \left[\Gamma\left(\frac{r}{l_{max}}, 3 - D_B\right) - \Gamma\left(\frac{r}{l_{min}}, 3 - D_B\right) \right] \quad [2]$$

where r is the spatial separation, $\Gamma(x, a)$ is the upper incomplete gamma function, and l_{min} and l_{max} characterize the lower and upper length scales of fractality, respectively. D_B is the effective chromatin packing scaling, a model parameter that describes the shape of B_ρ and is related to *D*, the true chromatin packing scaling. $\sigma_\rho^2 \frac{D_B - 3}{{l_{max}}^{D_B-3} - {l_{min}}^{D_B-3}}$ is the normalization factor of this ACF model, such that B_ρ(r = 0) is σ_ρ^2, the variance of mass density. We tested the validity of B_ρ to represent the ACF of chromatin mass density by fitting the model to experimentally derived ACFs from ChromTEM (50nm sections). For both A549 and BJ cells, the modified ACFs match the experimental ACFs with marginal errors (median R^2 of 0.985 over all samples for the fitting range of r between 50-200nm) (Fig. S9A), demonstrating the flexibility of this model.

Because of the chosen model, B_ρ it is not purely power law up to l_{max} but rather to some distance smaller than l_{max}. To account for this, we calculate the input model parameter l_{max} using the following formula to correct for the desired power-law maximum point, $l_{\max\_pl}$:

$$l_{max} = \left[\frac{N_f D_B \left[1 - \left(\frac{l_{min}}{l_{\max\_pl}} \right)^{3-D_B} \right]}{(3-D_B)\left[1 - \left(\frac{l_{min}}{l_{\max\_pl}} \right)^{D_B} \right]} \right]^{1/D_B} \quad [3]$$

In order to numerically establish the relationship between D_B and D, for each D_B, we generated B_ρ by computing l_{max} from [3]: choosing physiological values of N_f, setting $l_{min} = 1nm$, and starting with an estimate of $l_{\max\_pl} = l_{min} {N_f}^{1/D_B}$. Then, using linear regression, we fit B_ρ to r^{D-3} within the range of $\frac{l_{max}+l_{min}}{100}$ to $\frac{l_{max}+l_{min}}{100} + 0.1$ to compute D (Fig. S9B). Importantly, while D_B can range from 1 to 4, D can only physically take on values between 5/3 and 3 for a topologically unconstrained polymer in thermodynamic equilibrium. We notice that $D_B \approx D$ for all physiological values of D except for D approaching 3.

Calculating chromatin packing scaling D from PWS signal Σ^2

Within the nucleus, chromatin is the major contributor to PWS signal as most other macromolecules and physicochemical elements (i.e. ions) that also comprise the nuclear environment are below the length-scale sensitivity of PWS, which is 20-300nm, as the size of proteins is usually on the order of a few nanometers (*56*). In order to establish a direct relationship between the chromatin packing scaling D from PWS spectral variance Σ^2, we first express Σ^2as a function of the effective chromatin packing scaling D_B, then numerically convert to D. Next, we utilize the relationship between spectral variance and the spatial ACF: $\Sigma^2 \propto \left[B_\rho(r) \otimes T(r) \right]|_{r=0}$, denoted by the convolution ($\otimes$) between the ACF and a smoothing function (T) characterized by the microscope's NA and the source spectrum (*57*), evaluated at r = 0. It is clear that Σ^2 is linearly related to the ACF, and a linear decomposition of the ACF would result in a linear addition of Σ^2.

Employing the Laplace transform, we expanded the modified power-law ACF $B_\rho(r, D_B, l_{min}, l_{max})$ to a sum of weighted exponential functions, each with a characteristic decay length within the fractal regime [4].

$$B_\rho(r) = \int_{l_{min}}^{l_{max}} P(l_c, D_B) e^{-r/l_c} \, dl_c \quad [4]$$

Here, e^{-r/l_c} is a series of exponential basis functions with varying l_c, the characteristic length that modulates the speed of decay. P contains the weights for each exponential basis in the form of a continuous probability distribution function. P can be obtained by the normalized inverse Laplace transform. Putting equation [4] into the following form: $B_\rho(r) = \int_0^\infty f(t)\, e^{-rt} dt$, allows the calculation of P using the inverse Laplace through a simple change of variable, as shown in equation [5]. Furthermore, P must be normalized to sum to unity within the fractal regime:

$$P(l_c, D_B) = f\left(\frac{1}{t}\right)/t^2 \Big/ \int_{1/l_{max}}^{1/l_{min}} f\left(\frac{1}{t}\right)/t^2 \, dt = {l_c}^{D_B-4} \frac{D_B-3}{({l_{max}}^{D_B-3} - {l_{min}}^{D_B-3})} \quad [5]$$

Governed by the unitarity of the Fourier transform from spectral to spatial variance (Parseval's theorem), we can rewrite equation [4] in the spectral space while maintaining the same weighting function *P*. From [4], replacing $B_\rho(r)$ with $\Sigma^2(D_B)$ and e^{-r/l_c} with $\Sigma_e^2(l_c)$, the spectral variance measured from an exponential ACF, we obtain the relationship between PWS signal Σ^2 and the effective chromatin packing scaling D_B:

$$\Sigma^2(D_B) = \int_{l_{min}}^{l_{max}} P(l_c, D_B)\, \Sigma_e^2(l_c)\ dl_c \qquad [6]$$

Considering the experimental setup of a PWS microscopy (Materials and Methods: PWS imaging), $\Sigma_e^2(l_c)$ has a closed-form solution for an exponential basis function with a characteristic length l_c :

$$\Sigma_e^2(l_c) = \frac{2R^2\sigma_{n_\Delta}^2}{\pi} \frac{l_c^3 k^4 LNA^2}{[1+k^2 l_c^2(4+NA^2)](1+4k^2 l_c^2)} \qquad [7]$$

In [7], *R* is the product of the forward and reverse Fresnel transmission and reflection coefficients at the cell/glass interface, normalized by the reflectance coefficient of the reference (glass/media) interface: $\frac{4\, n_{nucleus}\, n_{glass}(n_{glass} - n_{nucleus})}{(n_{glass} + n_{nucleus})^3} \frac{(n_{glass} + n_{media})^2}{(n_{glass} - n_{media})^2}$, k is the center wavelength in vacuum, *NA* is the collection numerical aperture in air, *L* is the effective thickness of the sample, determined by the minimum of either the optical cell thickness or the depth of field (DOF), and σ_n^2 is the variance of refractive index (RI) fluctuations within the nucleus .

Next, we estimated the RI of the nucleus $n_{nucleus}$ from the densities of these nuclear components through the Gladstone-Dale equation:

$$n_{nucleus}(\phi) = n_0 + \alpha\rho_{chromatin}\phi + \alpha\rho_{MC}\phi_{MC} \qquad [8]$$

where n_0 is the RI of water in the wavelength range used; $\alpha = 0.18\ \frac{cm^3}{g}$ is the RI increment and is constant for all macromolecules that contribute to the spectral signal (*58*); $\rho_{chromatin}$ and ρ_{MC} are the densities of chromatin and MCs, ϕ is the chromatin volume concentration (CVC), and ϕ_{MC} is the crowding density of MCs. As most of the MCs we consider are proteins and nucleic acids, we used ρ_{MC} = 1.25 $\frac{g}{cm^3}$, the average density of pure, dehydrated proteins (*59*). We further estimated $\rho_{chromatin}$ to be 0.555 $\frac{g}{cm^3}$ by approximating the weight and total volume occupied by a single nucleosome and its linker DNA. We inputted a series of ϕ between 0.12 and 0.55, within the physiological range of chromatin volume concentration reported by ChromEMT for interphasic nuclei (*8*). Finally, we estimate $\phi_{MC} = \phi_{MC_{max}}(1-\phi)$, where $\phi_{MC_{max}}$ = 0.05 and is the maximum concentration occupied by MCs, and thus ϕ_{MC} is proportional to the volume unoccupied by chromatin.

We estimated the standard deviation of RI fluctuations σ_n by assuming ϕ follows a binomial distribution:

$$\sigma_n = \sqrt{\phi(1-\phi)}\,[\, n_{nucleus}(\phi = 1) - n_{nucleus}(\phi = 0)\,] \qquad [9]$$

We numerically calculated a series of $\Sigma(D_B)$ for varying D_B by inputting physiologically relevant values for ϕ and N_f, and computing $n_{nucleus}$, and σ_n from equations [8], [9] , respectively. Next, we input these values into equations [5] and [7] to compute P and Σ_e^2 as inputs to equation [6]. Importantly, the relationship between Σ and D_B can be accurately represented by a linear approximation. For physiologically relevant values ($\phi = 0.32$, $N_f = 1.0$Mbp), we obtain

$$\Sigma(D_B) \approx A(D_B - D_0), \qquad [10]$$

with fitted values of A = 0.13, $D_0 = 1.46$, and corresponding $R^2 = 0.999$, although this model does not change significantly for other physiologically relevant values of N_f and ϕ.

Finally, we scanned through an exhaustive range of possible D values and inputted the system incident NA of 0.55 and collection NA of 1.49 to generate a numerical relationship describing $\Sigma(D)$ as a function of ϕ and N_f. The range of N_f values displayed encapsulates the extreme values for packing domain size measured by ChromSTEM, which we have shown exhibits fractal behavior. For calculations performed in calculating D from Σ in the main text, we used ϕ = 0.32 and N_f = 1.0Mbp. As evident in Fig. S9C, the inversion, allowing for the calculation of D given experimentally measured Σ, is possible due to the monotonicity of the relationship. We also notice the relationship between Σ and D is relatively consistent, even considering the extreme limits of physiologically relevant ϕ and N_f.

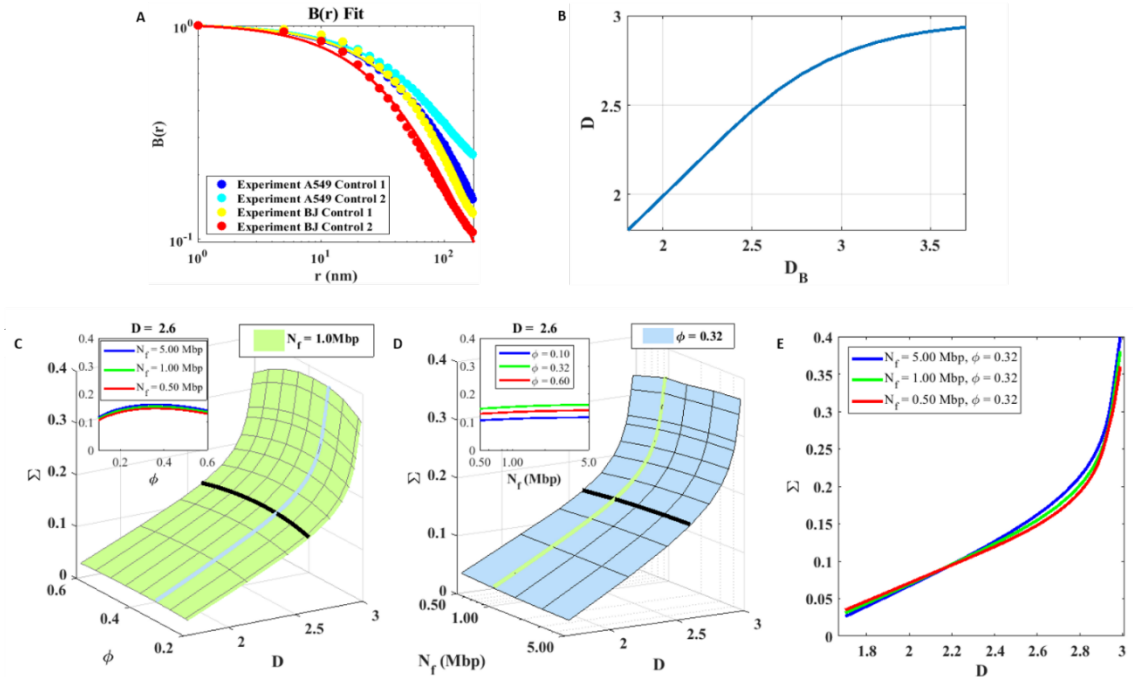

Fig. S9. Calculating *D* from *Σ*. (**A**) Comparing B_ρ(r) to representative experimental ACF of chromatin density calculated from ChromTEM data for A549 and BJ cells. For these four examples, the normalized model, shown as solid lines, fits the experimental data with only a small margin of error. (**B**) The numerically computed relationship between D and D_B for the modified power-law B_ρ defined in equation [1]. (**C**) Surface plot showing Σ vs D and ϕ for a fixed N_f of 1.0Mbp and under varying physiologically relevant conditions and fixed D = 2.6 for N_f (denoted

by the black line and expanded in inset). (**D**) Surface plot showing Σ vs D and N_f for ϕ of 0.32, and for varying physiologically relevant values of ϕ for a fixed D = 2.6 (denoted by the black line and expanded in inset). (**E**) 2D plot of Σ vs D for fixed ϕ and varying N_f. Blue and red lines are plotted at the extreme ranges of physiologically relevant values for N_f, while green shows mapping used in the conversion of PWS signal Σ to reported D values for this work.

REFERENCES AND NOTES

1. J. E. Phillips-Cremins, M. E. G. Sauria, A. Sanyal, T. I. Gerasimova, B. R. Lajoie, J. S. K. Bell, C.-T. Ong, T. A. Hookway, C. Guo, Y. Sun, M. J. Bland, W. Wagstaff, S. Dalton, T. C. McDevitt, R. Sen, J. Dekker, J. Taylor, V. G. Corces, Architectural protein subclasses shape 3D organization of genomes during lineage commitment. *Cell* **153**, 1281–1295 (2013).

2. E. J. Clowney, M. A. LeGros, C. P. Mosley, F. G. Clowney, E. C. Markenskoff-Papadimitriou, M. Myllys, G. Barnea, C. A. Larabell, S. Lomvardas, Nuclear aggregation of olfactory receptor genes governs their monogenic expression. *Cell* **151**, 724–737 (2012).

3. J. S. Becker, R. L. McCarthy, S. Sidoli, G. Donahue, K. E. Kaeding, Z. He, S. Lin, B. A. Garcia, K. S. Zaret, Genomic and proteomic resolution of heterochromatin and its restriction of alternate fate genes. *Mol. Cell* **68**, 1023–1037.e15 (2017).

4. P. C. Taberlay, J. Achinger-Kawecka, A. T. L. Lun, F. A. Buske, K. Sabir, C. M. Gould, E. Zotenko, S. A. Bert, K. A. Giles, D. C. Bauer, G. K. Smyth, C. Stirzaker, S. I. O'Donoghue, S. J. Clark, Three-dimensional disorganization of the cancer genome occurs coincident with long-range genetic and epigenetic alterations. *Genome Res.* **26**, 719–731 (2016).

5. P. Panikker, S.-J. Xu, H. Zhang, J. Sarthi, M. Beaver, A. Sheth, S. Akhter, F. Elefant, Restoring Tip60 HAT/HDAC2 balance in the neurodegenerative brain relieves epigenetic transcriptional repression and reinstates cognition. *J. Neurosci.* **38**, 4569–4583 (2018).

6. Y. Nishino, M. Eltsov, Y. Joti, K. Ito, H. Takata, Y. Takahashi, S. Hihara, A. S. Frangakis, N. Imamoto, T. Ishikawa, K. Maeshima, Human mitotic chromosomes consist predominantly of irregularly folded nucleosome fibres without a 30-nm chromatin structure. *EMBO J.* **31**, 1644–1653 (2012).

7. M. Eltsov, K. M. MacLellan, K. Maeshima, A. S. Frangakis, J. Dubochet, Analysis of cryo-electron microscopy images does not support the existence of 30-nm chromatin fibers in mitotic chromosomes in situ. *Proc. Natl. Acad. Sci. U.S.A.* **105**, 19732–19737 (2008).

8. H. D. Ou, S. Phan, T. J. Deerinck, A. Thor, M. H. Ellisman, C. C. O'Shea, ChromEMT: Visualizing 3D chromatin structure and compaction in interphase and mitotic cells. *Science* **357**, eaag0025 (2017).

9. A. D. Schmitt, M. Hu, B. Ren, Genome-wide mapping and analysis of chromosome architecture. *Nat. Rev. Mol. Cell Biol.* **17**, 743–755 (2016).

10. E. Lieberman-Aiden, N. L. van Berkum, L. Williams, M. Imakaev, T. Ragoczy, A. Telling, I. Amit, B. R. Lajoie, P. J. Sabo, M. O. Dorschner, R. Sandstrom, B. Bernstein, M. A. Bender, M. Groudine, A. Gnirke, J. Stamatoyannopoulos, L. A. Mirny, E. S. Lander, J. Dekker, Comprehensive mapping of long-range interactions reveals folding principles of the human genome. *Science* **326**, 289–293 (2009).

11. J. A. Beagan, J. E. Phillips-Cremins, On the existence and functionality of topologically associating domains. *Nat. Genet.* **52**, 8–16 (2020).

12. T. Nagano, Y. Lubling, T. J. Stevens, S. Schoenfelder, E. Yaffe, W. Dean, E. D. Laue, A. Tanay, P. Fraser, Single-cell Hi-C reveals cell-to-cell variability in chromosome structure. *Nature* **502**, 59–64 (2013).

13. Q. Szabo, D. Jost, J.-M. Chang, D. I. Cattoni, G. L. Papadopoulos, B. Bonev, T. Sexton, J. Gurgo, C. Jacquier, M. Nollmann, F. Bantignies, G. Cavalli, TADs are 3D structural units of higher-order chromosome organization in *Drosophila*. *Sci. Adv.* **4**, eaar8082 (2018).

14. T. Nozaki, R. Imai, M. Tanbo, R. Nagashima, S. Tamura, T. Tani, Y. Joti, M. Tomita, K. Hibino, M. T. Kanemaki, K. S. Wendt, Y. Okada, T. Nagai, K. Maeshima, Dynamic organization of chromatin domains revealed by super-resolution live-cell imaging. *Mol. Cell* **67**, 282–293.e7 (2017).

15. B. Bintu, L. J. Mateo, J.-H. Su, N. A. Sinnott-Armstrong, M. Parker, S. Kinrot, K. Yamaya, A. N. Boettiger, X. Zhuang, Super-resolution chromatin tracing reveals domains and cooperative interactions in single cells. *Science* **362**, eaau1783 (2018).

16. A. N. Boettiger, B. Bintu, J. R. Moffitt, S. Wang, B. J. Beliveau, G. Fudenberg, M. Imakaev, L. A. Mirny, C.-t. Wu, X. Zhuang, Super-resolution imaging reveals distinct chromatin folding for different epigenetic states. *Nature* **529**, 418–422 (2016).

17. S. S. P. Rao, M. H. Huntley, N. C. Durand, E. K. Stamenova, I. D. Bochkov, J. T. Robinson, A. L. Sanborn, I. Machol, A. D. Omer, E. S. Lander, E. L. Aiden, A 3D map of the human genome at kilobase resolution reveals principles of chromatin looping. *Cell* **159**, 1665–1680 (2014).

18. L. M. Almassalha, G. M. Bauer, W. Wu, L. Cherkezyan, D. Zhang, A. Kendra, S. Gladstein, J. E. Chandler, D. VanDerway, B.-L. L. Seagle, A. Ugolkov, D. D. Billadeau, T. V. O'Halloran, A. P. Mazar, H. K. Roy, I. Szleifer, S. Shahabi, V. Backman, Macrogenomic engineering via modulation of the scaling of chromatin packing density. *Nat. Biomed. Eng.* **1**, 902–913 (2017).

19. M. Cremer, T. Cremer, Nuclear compartmentalization, dynamics, and function of regulatory DNA sequences. *Genes Chromosomes Cancer* **58**, 427–436 (2019).

20. A. A. Sousa, A. A. Azari, G. Zhang, R. D. Leapman, Dual-axis electron tomography of biological specimens: Extending the limits of specimen thickness with bright-field STEM imaging. *J. Struct. Biol.* **174**, 107–114 (2011).

21. L. Cherkezyan, D. Zhang, H. Subramanian, I. Capoglu, A. Taflove, V. Backman, Review of interferometric spectroscopy of scattered light for the quantification of subdiffractional structure of biomaterials. *J. Biomed. Opt.* **22**, 30901 (2017).

22. P.-G. De Gennes, *Scaling Concepts in Polymer Physics* (Cornell Univ. Press, 1979).

23. Q. MacPherson, B. Beltran, A. J. Spakowitz, Bottom-up modeling of chromatin segregation due to epigenetic modifications. *Proc. Natl. Acad. Sci. U.S.A.* **115**, 12739–12744 (2018).

24. M. J. Uline, Y. Rabin, I. Szleifer, Effects of the salt concentration on charge regulation in tethered polyacid monolayers. *Langmuir* **27**, 4679–4689 (2011).

25. J. Nuebler, G. Fudenberg, M. Imakaev, N. Abdennur, L. A. Mirny, Chromatin organization by an interplay of loop extrusion and compartmental segregation. *Proc. Natl. Acad. Sci. U.S.A.* **115**, E6697-E6706 (2018).

26. P. J. Flory, The configuration of real polymer chains. *J. Chem. Phys.* **17**, 303–310 (1949).

27. L. A. Mirny, The fractal globule as a model of chromatin architecture in the cell. *Chromosome Res.* **19**, 37–51 (2011).

28. K. Falconer, *Fractal Geometry: Mathematical Foundation & Applications* (John Wiley and Sons, 1990).

29. A. Eid, A. Eshein, Y. Li, R. Virk, D. Van Derway, D. Zhang, A. Taflove, V. Backman, Characterizing chromatin packing scaling in whole nuclei using interferometric microscopy. *Opt. Lett.* **45**, 4810–4813 (2020).

30. S. Schoenfelder, P. Fraser, Long-range enhancer–promoter contacts in gene expression control. *Nat. Rev. Genet.* **20**, 437–455 (2019).

31. A. L. Sanborn, S. S. P. Rao, S.-C. Huang, N. C. Durand, M. H. Huntley, A. I. Jewett, I. D. Bochkov, D. Chinnappan, A. Cutkosky, J. Li, K. P. Geeting, A. Gnirke, A. Melnikov, D. McKenna, E. K. Stamenova, E. S. Lander, E. L. Aiden, Chromatin extrusion explains key features of loop and domain formation in wild-type and engineered genomes. *Proc. Natl. Acad. Sci. U.S.A.* **112**, E6456–E6465 (2015).

32. J. D. Halverson, J. Smrek, K. Kremer, A. Y. Grosberg, From a melt of rings to chromosome territories: The role of topological constraints in genome folding. *Rep. Prog. Phys.* **77**, 022601 (2014).

33. K. Huang, Y. Li, A. R. Shim, R. K. A. Virk, V. Agrawal, A. Eshein, R. J. Nap, L. M. Almassalha, V. Backman, I. Szleifer, Physical and data structure of 3D genome. *Sci. Adv.* **6**, eaay4055 (2020).

34. A. M. D'Ippolito, I. C. McDowell, A. Barrera, L. K. Hong, S. M. Leichter, L. C. Bartelt, C. M. Vockley, W. H. Majoros, A. Safi, L. Song, C. A. Gersbach, G. E. Crawford, T. E. Reddy, Pre-established chromatin interactions mediate the genomic response to glucocorticoids. *Cell Syst.* **7**, 146–160.e7 (2018).

35. The ENCODE Project Consortium, An integrated encyclopedia of DNA elements in the human genome. *Nature* **489**, 57–74 (2012).

36. H. Matsuda, G. G. Putzel, V. Backman, I. Szleifer, Macromolecular crowding as a regulator of gene transcription. *Biophys. J.* **106**, 1801–1810 (2014).

37. R. K. A. Virk, W. Wu, L. M. Almassalha, G. M. Bauer, Y. Li, D. VanDerway, J. Frederick, D. Zhang, A. Eshein, H. K. Roy, I. Szleifer, V. Backman, Disordered chromatin packing regulates phenotypic plasticity. *Sci. Adv.* **6**, eaax6232 (2020).

38. X. Darzacq, Y. Shav-Tal, V. de Turris, Y. Brody, S. M. Shenoy, R. D. Phair, R. H. Singer, *In vivo* dynamics of RNA polymerase II transcription. *Nat. Struct. Mol. Biol.* **14**, 796–806 (2007).

39. K. C. Palozola, G. Donahue, H. Liu, G. R. Grant, J. S. Becker, A. Cote, H. Yu, A. Raj, K. S. Zaret, Mitotic transcription and waves of gene reactivation during mitotic exit. *Science* **358**, 119–122 (2017).

40. V. Dileep, F. Ay, J. Sima, D. L. Vera, W. S. Noble, D. M. Gilbert, Topologically associating domains and their long-range contacts are established during early G1 coincident with the establishment of the replication-timing program. *Genome Res.* **25**, 1104–1113 (2015).

41. C. B. Hug, A. G. Grimaldi, K. Kruse, J. M. Vaquerizas, Chromatin architecture emerges during zygotic genome activation independent of transcription. *Cell* **169**, 216–228.e19 (2017).

42. B. R. Sabari, A. Dall'Agnese, A. Boija, I. A. Klein, E. L. Coffey, K. Shrinivas, B. J. Abraham, N. M. Hannett, A. V. Zamudio, J. C. Manteiga, C. H. Li, Y. E. Guo, D. S. Day, J. Schuijers, E. Vasile, S. Malik, D. Hnisz, T. I. Lee, I. I. Cisse, R. G. Roeder, P. A. Sharp, A.

K. Chakraborty, R. A. Young, Coactivator condensation at super-enhancers links phase separation and gene control. *Science* **361**, eaar3958 (2018).

43. T. Misteli, Beyond the sequence: Cellular organization of genome function. *Cell* **128**, 787–800 (2007).

44. N. Naumova, M. Imakaev, G. Fudenberg, Y. Zhan, B. R. Lajoie, L. A. Mirny, J. Dekker, Organization of the mitotic chromosome. *Science* **342**, 948–953 (2013).

45. S. F. Pedersen, C. Stock, Ion channels and transporters in cancer: Pathophysiology, regulation, and clinical potential. *Cancer Res.* **73**, 1658–1661 (2013).

46. Q. Szabo, F. Bantignies, G. Cavalli, Principles of genome folding into topologically associating domains. *Sci. Adv.* **5**, eaaw1668 (2019).

47. K. C. Palozola, J. Lerner, K. S. Zaret, A changing paradigm of transcriptional memory propagation through mitosis. *Nat. Rev. Mol. Cell Biol.* **20**, 55–64 (2019).

48. N. C. Durand, M. S. Shamim, I. Machol, S. S. P. Rao, M. H. Huntley, E. S. Lander, E. L. Aiden, Juicer provides a one-click system for analyzing loop-resolution Hi-C experiments. *Cell Syst.* **3**, 95–98 (2016).

49. J. Schindelin, I. Arganda-Carreras, E. Frise, V. Kaynig, M. Longair, T. Pietzsch, S. Preibisch, C. Rueden, S. Saalfeld, B. Schmid, J.-Y. Tinevez, D. J. White, V. Hartenstein, K. Eliceiri, P. Tomancak, A. Cardona, Fiji: An open-source platform for biological-image analysis. *Nat. Methods* **9**, 676–682 (2012).

50. J. R. Kremer, D. N. Mastronarde, J. R. McIntosh, Computer visualization of three-dimensional image data using IMOD. *J. Struct. Biol.* **116**, 71–76 (1996).

51. D. Gursoy, F. De Carlo, X. Xiao, C. Jacobsen, TomoPy: A framework for the analysis of synchrotron tomographic data. *J. Synchrotron Radiat.* **21** (Pt. 5), 1188–1193 (2014).

52. B. Schmid, J. Schindelin, A. Cardona, M. Longair, M. Heisenberg, A high-level 3D visualization API for Java and ImageJ. *BMC Bioinformatics* **11**, 274 (2010).

53. T. G. Dewey, *Fractals in Molecular Biophysics (Topics in Physical Chemistry)* (Oxford University Press, 1998).

54. M. Xu, R. R. Alfano, Fractal mechanisms of light scattering in biological tissue and cells. *Opt. Lett.* **30**, 3051–3053 (2005).

55. C. J. R. Sheppard, Fractal model of light scattering in biological tissue and cells. *Opt. Lett.* **32**, 142–144 (2007).

56. R. Phillips, J. Kondev, J. Theriot, H. Garcia, *Physical Biology of the Cell* (Garland Science, 2012).

57. L. Cherkezyan, I. Capoglu, H. Subramanian, J. D. Rogers, D. Damania, A. Taflove, V. Backman, Interferometric spectroscopy of scattered light can quantify the statistics of subdiffractional refractive-index fluctuations. *Phys. Rev. Lett.* **111**, 033903 (2013).

58. H. Zhao, P. H. Brown, P. Schuck, On the distribution of protein refractive index increments. *Biophys. J.* **100**, 2309–2317 (2011).

59. H. Fischer, I. Polikarpov, A. F. Craievich, Average protein density is a molecular-weight-dependent function. *Protein Sci.* **13**, 2825–2828 (2004).